Experimentally-informed lattice model to simulate the fiber pull-out behavior at the microscale

Gan, Yidong; Yang, Shen; He, Shan; Šavija, Branko

DOI
10.1016/j.conbuildmat.2024.136839

Publication date
2024

Document Version
Final published version

Published in
Construction and Building Materials

Citation (APA)
Gan, Y., Yang, S., He, S., & Šavija, B. (2024). Experimentally-informed lattice model to simulate the fiber pull-out behavior at the microscale. *Construction and Building Materials*, *436*, Article 136839. https://doi.org/10.1016/j.conbuildmat.2024.136839

Construction and Building Materials 436 (2024) 136839

Contents lists available at ScienceDirect

Construction and Building Materials

journal homepage: www.elsevier.com/locate/conbuildmat

Experimentally-informed lattice model to simulate the fiber pull-out behavior at the microscale

Yidong Gan [a], Shen Yang [a,*], Shan He [b,*], Branko Šavija [b]

[a] School of Civil and Hydraulic Engineering, Huazhong University of Science and Technology, Wuhan 430074, China
[b] Microlab, Faculty of Civil Engineering and Geosciences, Delft University of Technology, Delft 2628 CN, the Netherlands

ARTICLE INFO

Keywords:
Engineered cementitious composites
Fiber pull-out
Lattice fracture model
Interfacial transition zone
Microstructure

ABSTRACT

Engineered cementitious composite (ECC) is widely employed in engineering due to its high toughness and ductility. The Interfacial Transition Zone (ITZ) between the fibers and the matrix plays a vital role in influencing the strength and durability of ECC. This study introduces a numerical method to simulate fiber pull-out behaviors, specifically the fiber debonding and slipping. A birth-death method is proposed to account for the mechanical transition from fiber debonding stage to slipping stage. The contributions of various phases in the ITZ are explicitly considered. Furthermore, nanoindentation tests and Backscattered Electron (BSE) imaging were conducted to determine the microstructures of ITZ and local mechanical properties of each phase within the ITZ. A series of fiber pullout experiments with polyvinyl alcohol (PVA) fibers were conducted to calibrate and validate the model. Subsequently, the validated model was employed to explore the influence of w/c ratios, fiber orientations and bonding properties on the interfacial behavior. The microstructure-informed model proposed herein effectively predicts fiber pull-out behavior, facilitating a thorough exploration of fracture mechanisms throughout the pull-out process, and serves as the basis for multiscale modeling of ECC.

1. Introduction

Engineered cementitious composite (ECC) is widely used due to its high toughness, pre-peak tensile ductility, and the presence of multiple narrow microcracks [1–4]. The toughness and formation of multiple cracks in ECC rely on the incorporation of fibers, specifically high-performance polymer micro-fibers. When cracks appear around the fibers, the crack-bridging effect of the fibers helps maintain the strength of the composite and enhance its toughness. Therefore, when designing ECC, special consideration should be directed towards incorporating fibers and ensuring robust adhesion between fibers and concrete.

Mechanical interaction between fibers and the matrix depends on the ITZ microstructure [5–10]. There is a significant difference in the microstructure between the fiber-concrete ITZ and the bulk concrete matrix. This difference is attributed to the wall-effect phenomenon present at the fiber locations in the concrete [4,7,11,12]. The wall-effect causes a local increase in the water-cement ratio and enhances hydration, leading to higher porosity in the ITZ. Scrivener et al. [12] noted that the thickness of the ITZ was less than 50 μm. It is well known that the microstructure of the ITZ is important for the pulling-out behaviors of the fibers. The hydration products in contact with the fibers affect the formation of chemical bonds, and the local pore structure influences stress concentrations and triggers the crack initiation and propagation, thus affecting the slip strength and slip-hardening behavior of fiber at the slipping stage [13].

In general, the evaluation of the adhesion between fibers and concrete is conducted through single-fiber pull-out tests [8,14,15]. Several effects have been investigated, such as matrix, fiber type, fiber inclination, etc. [16–18]. Kanda and Li [19] categorized the outcomes of single-fiber pull-out tests into two phases: the debonding and the slipping process. The debonding stage is due to the chemical bond between the hydration products and the fiber, characterized by the absence of significant deformation [20]. During the slipping process, load transfer from the fiber to the matrix occurs solely through friction [21]. Kanda and Li [19] conducted single fiber pull-out bond tests with different w/c ratios. The results showed that the chemical bond strength at the debonding stage is relatively stable independent of the w/c ratio, contrary to the behavior of friction strength at the slipping stage. In addition, Robert et al. [18] tested the bonding characteristics of three different cement types and three types of fibers. The results revealed that the ettringite crystal structure, characterized by the increased rigidity and density, exhibited a higher capacity to transfer interfacial stress

* Corresponding authors.
E-mail addresses: ygan@hust.edu.cn (Y. Gan), yangshen@hust.edu.cn (S. Yang), S.He-2@tudelft.nl (S. He), B.Savija@tudelft.nl (B. Šavija).

https://doi.org/10.1016/j.conbuildmat.2024.136839
Received 25 March 2024; Received in revised form 21 May 2024; Accepted 28 May 2024
Available online 8 June 2024

from the fiber to the matrix—a crucial factor influencing friction strength. It was also found that the pull-out behaviors varied based on the interaction between the fiber type and the type of cement used. Specifically, PVA fibers demonstrated a significantly lower strain capacity compared to polypropylene (PP) fibers and steel fibers, particularly in establishing a high-strength chemical bond with the matrix, with failure predominantly occurring near the fiber tip. Besides the fiber types, PVA fibers as the common fiber embedded in ECC are often treated to reduce hydrophilicity for more strain hardness and ductility. Li et al. [19,22] performed fiber pull-out experiments to assess the characteristics of hydrophilic fiber-matrix contact and applied oil coating to the fiber surface to lower the interface bond. The coating results shows that oil is effective in counteracting the excessive chemical bond and facilitating the slipping-hardening effect for PVA fibers in cementitious composites. Meanwhile, Arain et al. [23] also employed various oiling agents to enhance the surface of PVA fibers locally. The diverse oiling treatments proved highly effective, significantly reducing the chemical debonding energy by 50–80 % compared to untreated PVA fibers. Curosu et al. [24] carried out experiments involving the chemical surface modification of PVA fibers. The findings revealed that the fiber-matrix adhesion of the modified fibers is significantly lower compared to the as-received oiled and non-oiled fibers.

It has been recognized that the fiber inclination also influences fiber pull-out behaviors on the friction strength, referred to as fiber apparent strength by Zhang and Li [17]. Curosu et al. [3] studied the impact of fiber inclinations on crack-opening relationships in various strain-hardening cementitious composites (SHCC). Curosu introduced dispersed fibers into the matrix during fiber pull-out tests, revealing that the impact of fiber orientation on pull-out behavior largely depends on the matrix type, whether plain or fiber-reinforced. Furthermore, specimens incorporating polyethylene fibers indicate that those embedded in a fiber-reinforced matrix exhibit stronger bond strength compared to those in a plain matrix. Conversely, specimens incorporating PVA fibers exhibit contrasting behavior.

In addition to experiments, several researchers investigate the bonding behaviors using analytical and numerical methods [25–29]. To improve the understanding of fiber pull-out and the matrix failure, Lin et al. [27] conducted a simulation of quasi-static fiber pushout employing a cohesive volumetric finite element scheme. The numerical analysis was segmented into two phases: the debonding process and the pull-out process. The debonding process was based on the cohesive zone model, while the pull-out process was simulated using the Coulomb-friction model. Within the pull-out process, the cohesive zone model incorporated a constitutive relation describing the tractions exerted on the interface in relation to the corresponding interfacial separation. Similarly, Tsai et al. [28] employed the same interface separation models. They integrated the models through node-to-node contact detection for cohesive debonding and node-to-surface contact detection for frictional sliding. This mixed model was capable of simulating the entire process, successfully reproducing fiber pull-out that involved plastic deformation within the fiber. While the previously mentioned model took into account cohesive contact at the interface, the effect of ITZ was not explicitly analyzed but rather considered in the equations within node and surface contacts. In a study of Li and Mobasher [29], they defined the ITZ as a third phase characterized by lower stiffness and strength compared to both the matrix and the fiber. The failure condition of the interface was represented by a biaxial yield surface, with interfacial shear strength taken into account during the debonding stage. The results indicated that the finite element simulation aligned with the experimental findings regarding debonding strength. However, the pull-out force during the slipping stage was found to be lower than the experimental results, and the stiffness of the fiber pull-out response was significantly overestimated using the finite element method (FEM). Likewise, Ellis et al. [30] investigated the fiber pull-out behavior using an ITZ thickness of 50 μm. They used a 3D finite element model at the scale of a single fiber to comprehend the mechanisms involved in debonding and slipping during the quasi-static pull-out of twisted fibers from cementitious materials. The model effectively replicates physical phenomena pertinent to the extraction of fibers from the concrete matrix. Li et al. [25] simulated the fiber pull-out failure by FEM. This simulation integrated a discrete cohesive concept into the smeared phase-field method. By employing a phenomenologically defined cohesive traction-separation law to model the interaction between the fiber and matrix, the numerical simulations successfully reproduced the characteristics observed in the experiments. Although previous models have made great progress in simulating fiber pull-out behavior, ITZ as the key determinant is often considered as homogenized phase in simulations. Within the ITZ, the chemical bond mainly determines the cohesive contact, particularly the hydrogen bonds formed between the fiber and different hydration phases. The composition of hydration products varies depending on the ITZ structure of different material compositions. Additionally, porosity and the strength of each phase in the ITZ affect the slipping behavior and pull-out strength of the fiber. Since the critical scale for studying and understanding the fracture behavior of ITZ is at the microscale [14,31–35], analyzing and understanding the fiber pull-out behavior is enhanced when considering the microstructure of ITZ. Furthermore, the numerical model attains greater reliability and generality when the realistic microstructure is considered [36–38].

The purpose of this paper is to establish a fiber pull-out model by considering the microstructure of the ITZ and use it to predict the two stages of fiber pull-out process. The first step involves single fiber pull-out experiments in order to calibrate and validate the numerical model. Furthermore, nanoindentation tests performed to determine the local mechanical properties of various cement phases, and BSE tests to obtain the realistic microstructure of ITZ. In the second step, a microstructure-informed lattice model simulating debonding and slipping stages of fiber pull-out is established based on the experimental results. The last step involves systematically analyzing the influences of w/c ratio, fiber inclination, and bond strength on debonding and slipping behaviors by utilizing the microstructure-informed lattice model.

2. Experiments

2.1. Materials

This investigation utilized CEM I 42.5 N Portland cement to formulate cement pastes with water-to-cement (w/c) ratios of 0.4. The PVA microfiber sourced from Kuraray (Japan), featuring a 1.2 % oiling coating by weight, which is a common constituent in ECC, was used. According to the manufacturer, the fiber has a nominal diameter of 39 μm. The oil coating acts as a hydrophobic barrier between the hydrophilic PVA surface and the cement-based matrix. Given the minimal thickness of the coating, it is improbable that the microstructure of the ITZ will be significantly affected by its presence.

2.2. Sample preparation

Two types of specimens were prepared for the experiments. For single fiber pullout tests, the specimen preparation adhered to the protocol outlined in our prior publication [39]. In brief, a continuous filament was trimmed to approximately 150 mm and embedded within the cement paste matrix. Following one day of curing, the hardened specimens were demolded and subjected to an additional 27 days of curing in lime-saturated water within a laboratory environment maintained at a temperature of 23 ± 3 °C. After curing, the specimens were precisely sawn into thin sections with 1 mm in thickness, each featuring a single fiber extruding from one side.

For BSE image analysis and nanoindentation, the same specimens utilized for single fiber pullout underwent further preparation steps. A comprehensive procedure is outlined in the Appendix of our previous publication [40]. To summarize, after slicing the specimens into thin

plates, an additional cutting was made approximately 20 microns away from the fiber. This adjustment aimed to facilitate epoxy impregnation into the pores within the ITZ region and aid in the polishing process. After hardening of the epoxy, the specimens underwent grinding to produce a longitudinal section intersecting the fiber's long axis. The final step involved surface polishing, adhering to a dedicated protocol detailed in [40].

2.3. Characterization techniques

2.3.1. Single fiber pullout test

The interface properties were determined using single fiber pullout tests following previous studies by Redon et al. [20]. A micromechanics-based model proposed by Lin et al. [41] was adopted to describe the bond properties through the notions of: (1) chemical bond strength G_d quantified by interfacial fracture toughness, (2) constant frictional bond strength τ_0 for small sliding, and (3) slip hardening coefficient β that characterizes the increasing effective frictional bond during large sliding (pullout) stage. The tests were performed by a test setup schematically shown as Fig. 1. Details of the test equipment employed can be found in our previous publication [39]. During the test, both the bottom surface of the thin specimen and the free end of the fibers were glued to two small metal blocks, which were then clamped with the actuator and the load cell. The pull-out process was carried out at a displacement rate of 0.005 mm/s. 10 specimens were tested for w/c ratio of 0.4, the results of which were then analyzed to determine the interface properties (*i.e.*, chemical bond G_d, frictional bond τ_0, and slip-hardening coefficient β) according to Eqs.1–3:

$$G_d = \frac{2(P_a - P_b)^2}{\pi^2 E_f d_f^3} \tag{1}$$

$$\tau_0 = \frac{P_b}{\pi d_f L_e} \tag{2}$$

$$\beta = (d_f/l_f)[(1/\tau_0 \pi d_f)(\Delta P/\Delta S')|_{S'\to 0} + 1] \tag{3}$$

where E_f, d_f and L_e are the elastic modulus [GPa], diameter [mm], and embedded length of PVA fiber [mm], respectively. $\Delta P/\Delta S'$ is the initial slope of the pullout load vs displacement. P_a is the load up to full debonded length and P_b is the load when the fiber begins to slip.

2.3.2. BSE image analysis

BSE analysis was performed under the BSE detector in an FEI QUANTA FEG 650 environmental SEM in high vacuum chamber condition. All specimens were coated with a roughly 10 nm thick layer of carbon before BSE examination. In a typical BSE image as shown in Fig. 2, the brightness of each pixel depends on the mean atomic number of the underlying phases. This allows pores, hydrated phases, and anhydrous phases to be differentiated on the basis of their grayscale value. The embedded fiber, which contains mainly the element of carbon, can be easily identified as a dark black rectangle. Epoxy filled pores could be seen also in dark black.

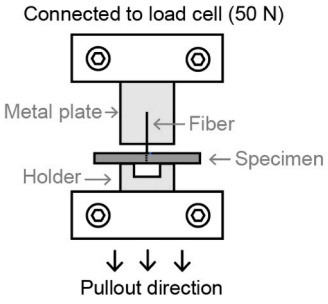

Fig. 1. Illustration of single fiber pull-out test.

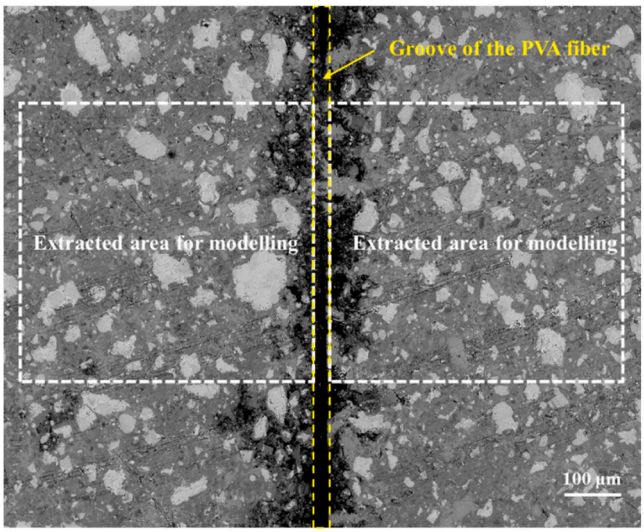

Fig. 2. BSE image of fiber pull-out specimen with w/c of 0.4.

To precisely analyze the individual phases, various methods for segmentation have been proposed [42–45]. In this study, a random forest machine learning model [46] was used for segmentation. The random forest machine learning algorithm builds multiple decision trees during training and combines their results to produce more accurate and stable predictions. The original training data were selected from BSE images. Five subsets were created by randomly sampling, with each subset used to train a different decision tree. The training dataset comprised over 300 samples for each phase. During the construction of each tree, a random subset of features, such as characteristic grayscale and morphology, is chosen for splitting a node. Each decision tree is grown to its maximum depth without pruning. The resulting learning model was trained better to identify the phases and was then applied to all specimens. The segmentation results were also validated through the testing results in literature. For instance, the volume fraction of pore, high-density of calcium-silicate-hydrate (HD C-S-H), low-density of calcium-silicate-hydrate (LD C-S-H), calcium hydroxide (CH) and anhydrous cement were 6.91 %, 41.13 %, 33.66 %, 9.18 % and 9.12 % respectively, with hydration degree of 80.1 %, when the w/c ratio is 0.4. The segment volume fraction results align closely with those reported by other researchers [34–36]. Wong and Buenfeld [45] derived the volume fractions of pore, hydration products and anhydrous cement as 21.6 %, 68.2 % and 10.1 % respectively, with hydration degree of 78.8 %. These results are consistent with the segment results obtained in this study. Similarly, Zhang et.al [37] calculated volume fraction of LD C-S-H in C-S-H to be 0.53. Additionally, Zhang and Gjørv [47] determined CH content to be 8.59 % by volume at a w/c ratio of 0.4.

2.3.3. Nanoindentation

The local mechanical properties for different phases were determined through Nanoindentation. These tests were performed by using a G200 Nanoindenter with a continuous stiffness method (CSM) module in the ITZ region at both sides of a microfiber. Each indent was made to a depth of 500 nm at a strain rate of 0.05 s-1. The modulus (or hardness) results of each indentation test were determined from the CSM indentation curves by averaging the hardness (or modulus) values between 100 nm and 500 nm indentation depth. The harmonic frequency and displacement of CSM oscillation are 45 Hz and 2 nm, respectively. In total, 600 nanoindentation points were tested around the fiber for the specimen with a w/c of 0.4. At each side, an array of 10 × 30 indentation at a spacing of 10 μm were performed to cover an area of 100 μm × 300 μm parallel to the fiber. The closest row of points to the fiber was positioned at a distance of 10 μm.

As suggested by previous studies [36,48], the continuous stiffness method was used to calculate the hardness and modulus utilizing the results of nanoindentation testing. Due to the significant variations in the mechanical properties of different phases within the heterogeneous microstructure, the calculation results exhibit a high degree of variability. Herein, Gaussian Mixture Model (GMM) was used to classify the results into categories for each phase. The results of modulus and hardness are shown in Fig. 3.

Based on research examining the relationship between hardness of nanoindentation result and strength of the relevant phase [36], the tensile strength is approximately 1/30 of the hardness. The compressive strength is considered as 10 times higher than the tensional strength. 8 specimens with different microstructures were considered in lattice model subjected to fiber pullout.

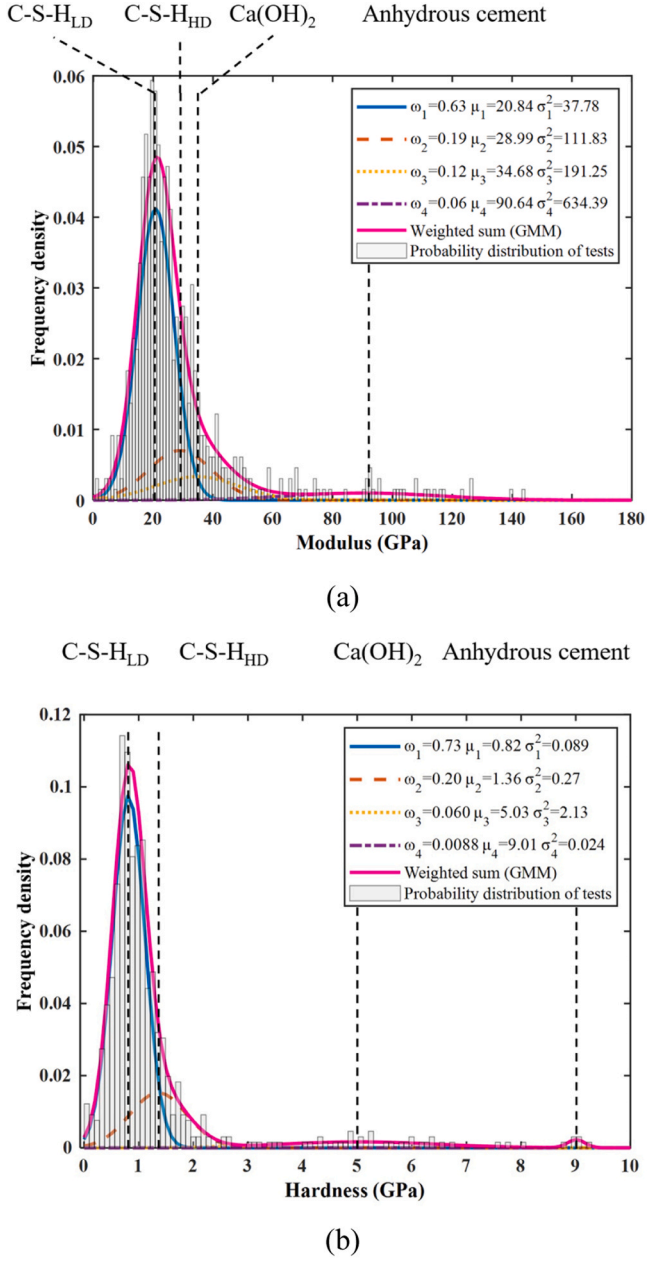

Fig. 3. Modulus (a) and hardness (b) GMM results of specimens with w/c ratio of 0.4.

3. Lattice modeling of fiber pull-out

3.1. Microstructure-informed lattice model

The current study utilizes the two-dimensional lattice fracture model to analyze the debonding and slipping stages during fiber pull-out process. The lattice model is a promising tool for simulating the fracture behavior of quasi-brittle material by calculating and removing the broken elements step by step [36,37]. The lattice network construction is depicted in Fig. 4. In this model, a network of cells is initially generated. Within each cell, a sub-cell is delineated where a node is randomly positioned. The ratio between the length of the sub-cell and the cell itself is defined as randomness [37]. Pore phase cells do not generate any lattice nodes. Then the lattice nodes in the neighboring cells are connected by lattice beam elements, forming a lattice network system capable of bearing loads. During each loading step, an element displaying the highest stress is selectively removed from the mesh. The lattice model has the capability to explicitly incorporate the microstructural heterogeneity and replicate the evolution of cracks, as well as stress-strain curves, in a manner consistent with experimental observations [36,37]. For the simulation of two stages in the fiber pull-out process, two different constitutive laws are assigned to the interface element. In the debonding stage, the interface element mimics the chemical bonding between the fiber and paste matrix, which shows elastic-brittle behavior. After the fracture of the chemical bond, all the interface elements were removed and the fiber was elevated to a new position. At this stage, new interface elements between the fiber and the matrix will be generated (see Fig. 6). These new elements exhibit higher resistances including high friction between the matrix and the fiber, and dowel action caused by the inclined deformation. The interface elements achieve unique functionality at different stages through different element mechanical properties shown at Table 1.

The ITZ microstructure is then mapped to the lattice model through the BSE result, as shown in Fig. 5. The lattice model has the same scale as the microstructure. In the model, the size of a lattice element is 1 μm, and the size of the model is 1040 μm in length and 600 μm in height. Every node is restricted within its sub-cell with a randomness of 0.5. After all the node positions are established, nodes will be connected to surrounding adjacent nodes by beam elements. And the cross sections of element are defined as circular.

Through the mapping relationship of ITZ microstructure and lattice modeling mesh, every node has a unique corresponding position in the microstructure. The microstructure was divided into anhydrous cement, C-H, HD C-S-H, LD C-S-H and pore. According to the corresponding position of every cement phase on 2-D plate, the nodes can be divided into four categories including anhydrous cement node, C-H node, HD C-S-H node and LD C-S-H node. Nodes in pores were deleted. The type of element can be determined by the types of its two nodes. The elements which belong to each phase are identified by the corresponding materials (i.e., A-A represents the element in anhydrous cement). Contact elements are generated between two phases (i.e., A-C represents the element across anhydrous cement and CH). Among the contact

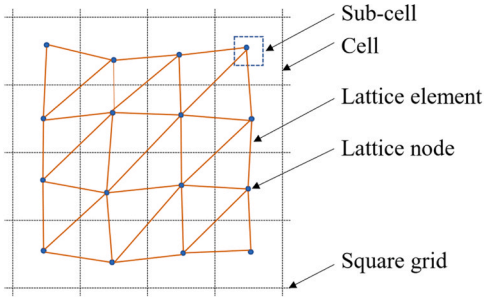

Fig. 4. Lattice network construction diagram.

Table 1
Classification of FCIE types and material properties during debonding and slipping stage.

Stage	Element Type	Phase 1	Phase 2	Modulus of Elasticity (GPa)	Tensional strength (MPa)
Debonding	F-HD	Fiber	HD C-S-H	18	45
	F-LD		LD C-S-H	13.5	27
Slipping	F-A	Fiber	Anhydrous cement	6	150
	F-C		C-H	4.5	90
	F-HD		HD C-S-H	0.5	10
	F-LD		LD C-S-H	0.5	6

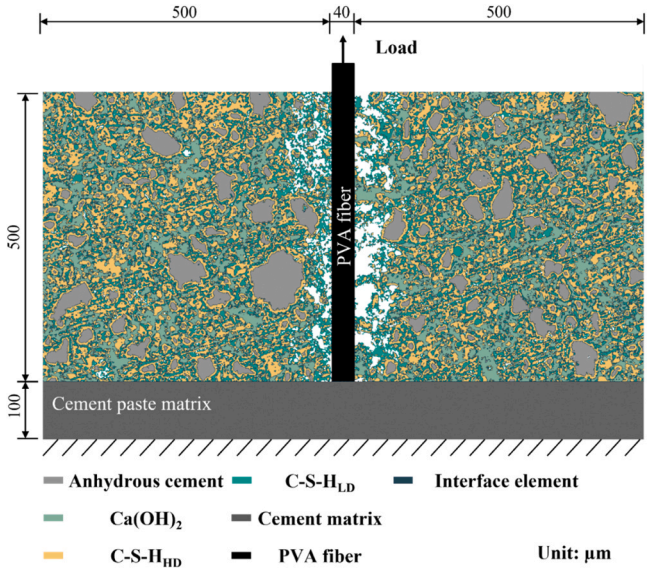

Fig. 5. Generation of lattice model including the microstructure of ITZ.

elements, the fiber-cement interface elements (FCIEs) can be classified into 5 types as listed in Table 1.

As shown in Fig. 5, the load is applied as a normal force exerted on the upper side of the fiber during both the debonding and slipping stages. The boundary conditions are represented by fixed support at the bottom of the specimen.

For the PVA fiber, the determination of material properties was based on experiments. Their material properties are given in Table 2. For the elements which connect different types of nodes, the tensile strength is decided by the weak phase, and the modulus of the element *i-j* are determined as Eq. (4).

$$\frac{2}{E_{ij}} = \frac{1}{E_i} + \frac{1}{E_j} \tag{4}$$

where E_{ij} is modulus of the element *i-j*, GPa, E_i is the modulus of cement phase at node *i*, GPa, E_j is the modulus of cement phase at node *j*, GPa.

Table 2
Mechanical properties assigned for different element types.

Element Type	Modulus of Elasticity (GPa)	Tensile strength (MPa)
Anhydrous cement	95.01	615.19
C-H	34.64	315.82
High density C-S-H	30.13	78.73
Low density C-S-H	19.97	53.26
Matrix	80	200
Fiber	41.1	1640

3.2. Birth-death method

Birth-death method is proposed herein to simulate the transition of fiber pull-out process from the debonding to the slipping stage. This method becomes effective after the failure of the fiber-matrix interface, during which all bonding elements are broken. Once all bonding elements have been eliminated, re-birth elements that represent the slipping behavior of the fiber are generated, as shown in Fig. 6. This assumption is rooted in the experimental observation that the failure of bond only occurs under small elastic deformations, while the slip of fiber is associated with large unrecoverable deformations. During the debonding stage, the interface elements experience breakage due to their low strength, until all interface elements are fractured. This breakage leads to irreversible deformation occurring before the complete elimination of all interface elements, establishing a new equilibrium where the balance is achieved through friction and loading. Simultaneously, the fiber is repositioned to a new location. According to the load-displacement curve (see Fig. 7), maximal deformations during debonding stage can be determined at the ultimate strength. The unrecoverable deformation is derived as the abscissa of the intersection point between the fitting line of the slipping curve and the x-axis. Empirically, based on data from 10 experiments, the ratio of eventual unrecoverable deformation to maximum deformation at the debonding stage is determined to be 53.84 ± 15.5 %. The interface elements, acting as the "death" elements, are subsequently removed from the model. New interface elements are then generated between fiber nodes and matrix nodes at the fiber's new position. These newly generated interface elements, termed "re-birth" elements, are utilized to simulate fiber slippage and are assigned distinct material properties to represent frictional effects. The material properties of interface elements employed during the debonding and slipping stages are given in Table 1. It is noted that, during debonding stage, a few cracks may generate in the matrix. The broken element shown in matrix are permanently removed.

After the transformation between death elements and birth elements was accomplished, the lattice slipping model analysis was conducted under the same load and boundary condition.

3.3. Calibration and validation of lattice model

In the experiment, the exposed fiber length is not well defined due to the measurement difficulties. The primary components of specimen displacement are the elastic stretching of the exposed fiber length and the debonded fiber segment [20,29]. To calibrate the length of the exposed fiber outside the matrix, the same microstructure was used to simulate the fiber pull-out behavior with the fiber length of 8 mm, 10 mm, 12 mm, and 14 mm, respectively. The stress-strain results from both the modeling and experiments are illustrated in Fig. 8. Based on the simulation results, the 10 mm exposed length of the fiber outside the matrix fit well with the majority of experimental results. Consequently, the 10 mm exposed length of fiber outside the matrix is used in the following modeling.

Besides, the strengths of FCIEs also need to be calibrated. FCIEs include F-A, F-C, F-HD, F-LD and F-M. The calibration includes the tensile strength and modulus of elasticity at both debonding and slipping stages. The calibration and validation processes are as follows [49]. The strength ratio of each FCIE is initially determined based on the proportion of corresponding strength of phase with which fiber is intact within the FCIE. The strengths of FCIEs are adjusted proportionally until the simulated results align with the experimental data. The material properties of the elements are preserved and applied to 8 specimens with distinct microstructures (FP1 to FP8), yielding results as depicted in the Fig. 9. The results demonstrate a satisfactory alignment of the model with the experimental data. The material properties of the elements are summarized in Table 1.

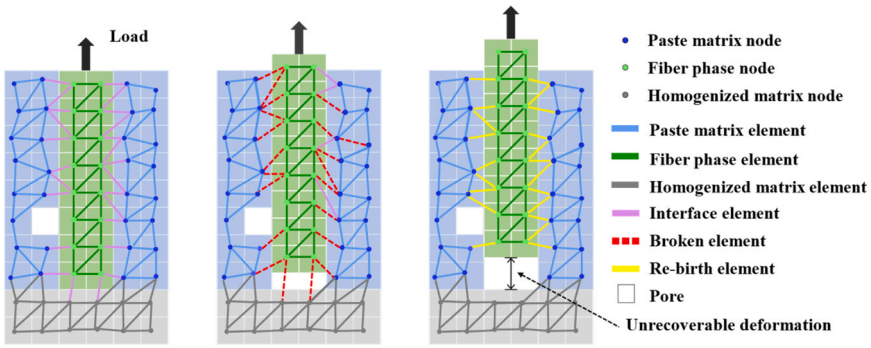

Fig. 6. Process of interface elements transition and structural status change with birth-death model.

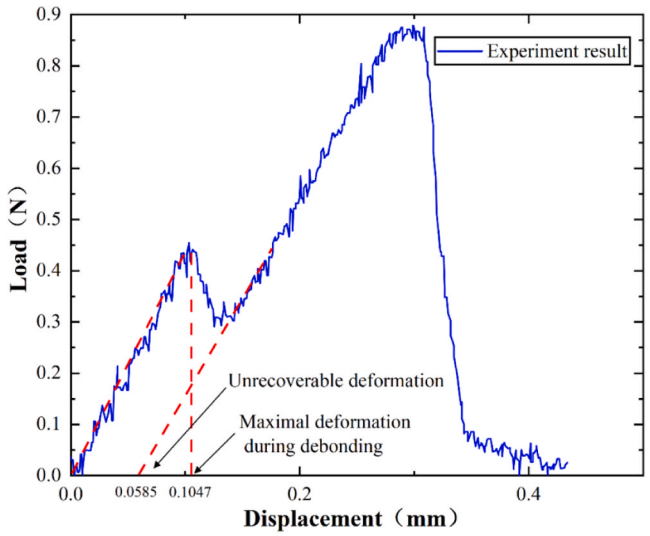

Fig. 7. Unrecoverable deformation in the load-displacement curve resulting from single fiber pull-out experiment with a w/c ratio of 0.4.

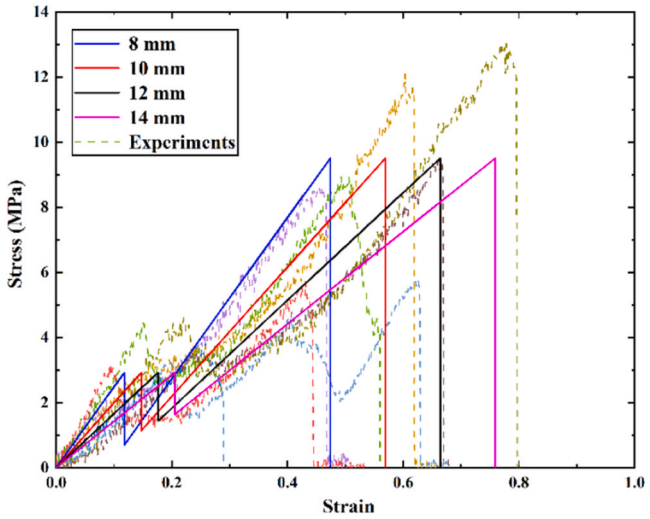

Fig. 8. Pull-out stress-strain curves from experiments under various exposed lengths of fiber and simulations under exposed fiber length of 8 mm, 10 mm, 12 mm, 14 mm with w/c ratio of 0.4.

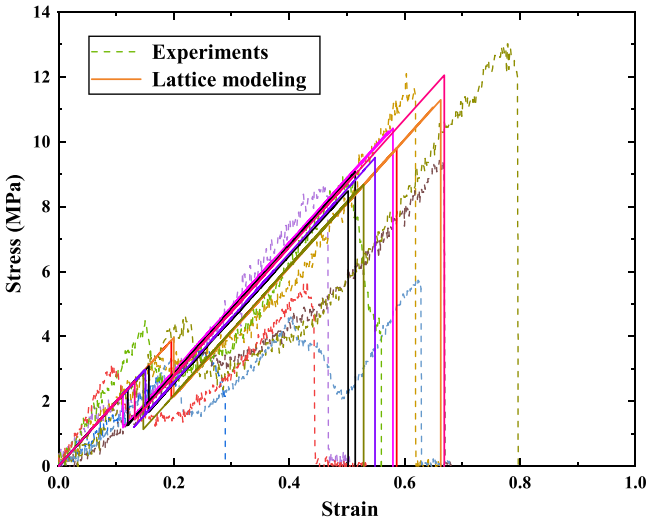

Fig. 9. Pull-out stress-strain curves from experiments and simulations with various microstructures under w/c ratio of 0.4.

4. Results and discussion

The results encompassed the experimental and numerical outcomes regarding the performance of individual fiber pull-out, debonding, and sliding stress, taking into account the influences of microstructure, w/c ratio, fiber inclination angle, and bond strength on PVA fiber pull-out behavior.

4.1. *Effect of microstructure*

The simulated stress-strain curves along with experimental results are shown in Fig. 10. It can be seen that the curve displays significant slipping hardening behavior and there are mainly two stages: debonding and slipping. The maximum stress in the debonding stage is approximately 3 MPa, denoted as the chemical bond strength [19], with a corresponding strain ranging from 0.15 to 0.2. Subsequently, the stress decreases to around 2 MPa termed as the fractional bond strength [20]. The slipping stage is characterized by friction process between the fiber and matrix, resulting in hardening behavior. Chemical bond strength τ_d, frictional pull-out strength τ_f and in-situ fiber pull-out strength σ_f are calculated according to Eqs. 5–7:

$$\tau_d = \frac{P_a}{\pi d_f L_e} \tag{5}$$

$$\tau_f = \frac{P_{\max}}{\pi d_f L_e} \tag{6}$$

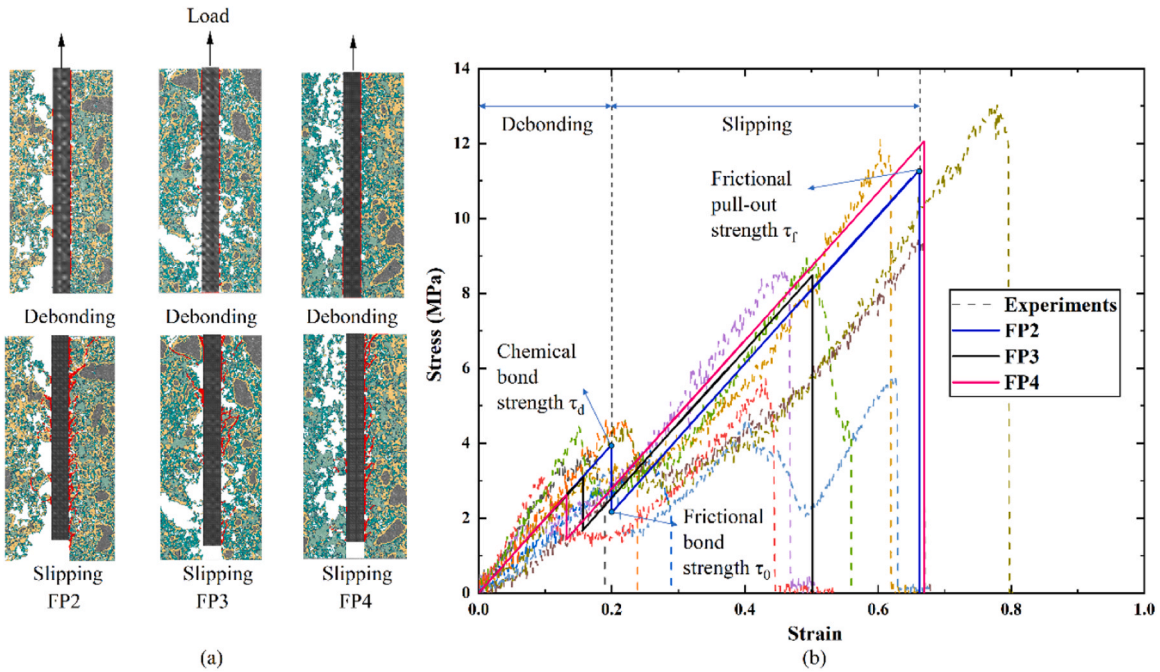

Fig. 10. (a) Fracture of elements in ITZ at the end of debonding and slipping (cracks are shown as red) and (b) stress-strain curves from experiments and simulations with the w/c of 0.4.

$$\sigma_f = \frac{P_{\max}}{\pi d_f^2 / 4} \tag{7}$$

where P_{max} is the fiber pull-out load at slipping stage, [N].

As shown in Table 3, the simulation results are consistent with that of experiment with w/c ratio of 0.4. It can be seen that the results exhibit large standard deviations especially in the chemical bond strength and frictional pull-out strength. The different microstructures surrounding the fiber influence the strength and failure patterns during fiber pull-out process. Furthermore, the exposed fiber in experiments generates elastic extension during pull-out process. The microstructure and exposed length of fiber contribute to the increased magnitude of the standard deviation.

The results in Table 4 illustrated the simulation results of specimens FP2, FP3, and FP4 with different microstructures. The results are consistent with the experimental data reported by Curosu et al. [3], which include an average frictional bond strength of 2.34 MPa and an in-situ strength of 677 MPa.

The microstructure of ITZ influences fracture patterns observed during both the debonding and slipping stages. As shown in Fig. 10 (a), most cracks observed during the debonding stage appear along the interface between the fiber and the matrix. As a result, factors affecting debonding strength include the quantities and the types of interface elements. As shown in Table 5, compared to FP2 and FP4, the quantities of interface elements between the fiber and the matrix are noticeably smaller in FP3. Additionally, concerning the types of crack elements, Table 5 provides the proportion of fracture element types. From the table, it can be observed that FP2 has a higher proportion of F-HD, and F-HD has the maximum debonding strength. Consequently, model FP2 has more contact elements and higher proportion of F-HD. FP2 exhibits significantly higher debonding strength than FP3 and FP4, as shown in Fig. 10.

In the slipping stage, fracture patterns are depicted in Fig. 10 (a). Contrary to the debonding stage, the strength of the interface elements between the fiber and matrix is higher, as evidenced by Table 1, leading to the emergence of broken elements within the matrix. A greater number of cracks is observed during the slipping stage, and these cracks extend into the matrix. Consequently, the strength during the slipping stage surpasses that of the debonding stage. Moreover, the microstructure within the ITZ directly influences the frictional strength during the

Table 3
Simulation and experiment results of specimens with w/c ratio of 0.4. Average values are given with standard deviations in parentheses.

Results	τ_d (MPa)	τ_0 (MPa)	τ_f (MPa)	σ_f (MPa)	G_d (J/m^2)	β
Simulation	3.00 (0.59)	1.57 (0.36)	9.92 (1.18)	495.88 (59.04)	1.07 (0.43)	2.00 (0.47)
Experiment	3.48 (0.86)	2.03 (0.58)	8.34 (2.69)	417.07 (134.71)	1.28 (0.89)	1.25 (0.31)

Note: τ_d represents chemical bond stress, τ_0 represents frictional bond strength, τ_f represents frictional pull-out strength, σ_f represents in-situ tensile strength, G_d represents chemical debonding energy.

Table 4
Simulation results of specimens with different microstructures (w/c 0.4).

Model	τ_d (MPa)	τ_0 (MPa)	τ_f (MPa)	σ_f (MPa)	G_d (J/m^2)	β
FP2	3.96	2.14	11.29	564.55	1.65	1.52
FP3	2.59	1.43	12.03	601.50	0.70	2.55
FP4	3.08	1.68	8.49	424.31	0.98	1.55

Table 5
The proportion of each FCIE and the total broken element numbers at the end of debonding of model FP2, FP3 and FP4 with w/c ratio of 0.4.

Element Type	FP2	FP3	FP4
F-HD	42.77 %	11.01 %	16.70 %
F-LD	36.94 %	62.20 %	54.47 %
F-C	8.83 %	9.64 %	16.06 %
F-A	1.91 %	0	0.27 %
Others	9.55 %	17.15 %	12.5 %
Broken element numbers	1100	800	1200

slipping stage. When the porosity is high and the proportion of low-density CSH is higher which has low strength, as illustrated in Fig. 10 (a), the frictional pull-out strength of the slipping stage diminishes. Conversely, in scenarios where the porosity in the ITZ is low, and the hydration product comprises a higher proportion of phases with high strength, such as high-density CSH and anhydrous cement particles, the energy required for crack initiation increases. Additionally, owing to the high strength of anhydrous cement and CH, cracks tend to disperse around anhydrous cement particles and penetrate deeper into the matrix, resulting in a higher strength during the slipping stage, as observed in Fig. 10 (a).

4.2. Effect of w/c ratio

The impact of the w/c ratio on fiber pull-out behavior during both the debonding and slipping stages has been examined. As discussed in Section 4.1, the microstructure of the ITZ significantly influences the strength and fracture patterns of fiber pull-out. Moreover, w/c ratio affects the formation of the microstructure on porosity and content of cement hydration. To evaluate the influence of the w/c ratio on the single-fiber pull-out test, nine models were generated. Each set of three models shared the same w/c ratio, with values of 0.3, 0.4, and 0.5. The simulation results closely align with experimental results, with the simulated in-situ strength averaging 417.07 MPa for a w/c ratio of 0.4. Experimental results fall within the range of 460 MPa to 560 MPa for a w/c ratio of 0.36 [23].

It can be observed from the Fig. 11 (b) that with the increase of w/c ratios from 0.3 to 0.5, chemical bond strength remains around 3 MPa. Kanda and Li [19] thought the chemical bond strength was relatively stable and independent of w/c ratio of matrix. The strength during the debonding stage is influenced by factors such as the quantity and the proportion of contact elements. Although there is not a significant difference in strength during the debonding stage, it is noteworthy that the strength tends to be relatively higher when the w/c ratio is 0.3.

During the slipping stage, the frictional pull-out strength significantly decreases with an increase in the w/c ratio. As shown in the Fig. 11 (a), when the w/c ratio is 0.5, the ITZ exhibits higher porosity and higher proportion of LD CSH. As a result, the frictional pull-out strength is low, and few cracks develop, with fractures occurring near the fiber. As the w/c ratio decreases to 0.4, the ITZ exhibits lower porosity and higher proportion of HD CSH. Comparing to w/c 0.5, the weak regions in the specimens become more resistant to fracture at w/c 0.4. Consequently, the frictional pull-out strength is higher, and fractures occur in areas farther from the fiber. In these new areas, broken elements typically consist of LD CSH elements and other elements surrounding anhydrous cement, as shown in Fig. 11 (a). When the w/c ratio decreases to 0.3, there is lower porosity, reduced hydration degree and a higher proportion of HD CSH. The microstructure in matrix is well-distributed and is hard to break. Therefore, more energy is required for fracture with a w/c ratio of 0.3 and frictional pull-out strength is higher. It should be noted that cracks in the specimen with a w/c ratio of 0.3 are distributed more densely in ITZ, extending from the top to the bottom.

4.3. Effect of fiber inclination

The lattice models with a w/c ratio of 0.4 at different angles of fiber inclination are depicted in Fig. 12. The simulation results of pull-out behaviors at different angles are presented in Table 6. In general, the average bond strength decreases with the increasing inclination angle. The Fig. 13 shows the in-situ tensile strength ratios at various angles relative to the in-situ tensile strength at 0°. The snubbing coefficient is calculated as 0.515. It is noteworthy that the snubbing coefficient in the experiments conducted by Kanda and Li [19] is 0.3, while Zhang and Li [17] derived it as 0.5 and Curosu [3] reported a value of 0.18.

To evaluate the influence of the fiber inclination angle on frictional pull-out strength and crack generation, different microstructures with fiber inclination angle of 0°, 30°, 45° and 60° were simulated. Two specimens with different microstructures were compared with the strength and crack details. As shown in Fig. 14. the chemical bond strength noticeably decreases with an increasing inclination angle in model FP1. At the slipping stage, the strength increases with the

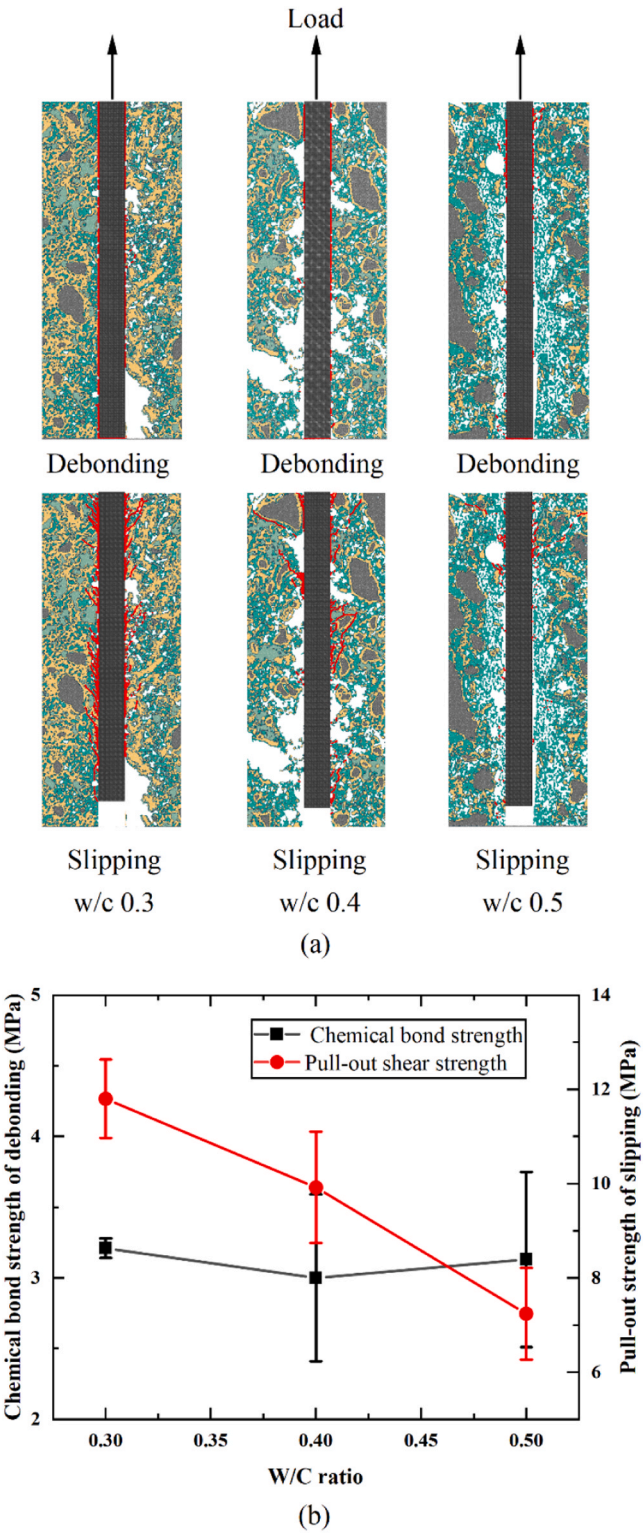

Fig. 11. (a) Fracture of elements in ITZ at the end of debonding and slipping stage and (b) chemical bond strength and frictional pull-out strength with w/c ratio from 0.3 to 0.5.

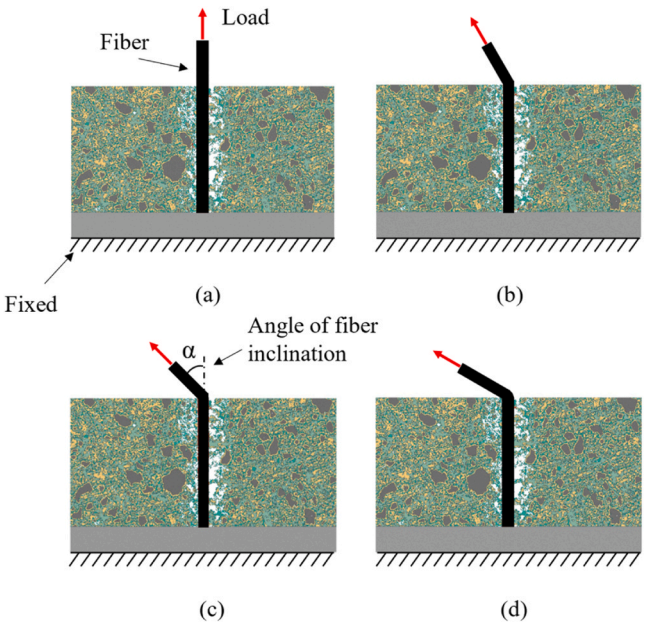

Fig. 12. Lattice model of FP1 with a w/c ratio of 0.4 at fiber inclination angle of: (a) 0°, (b) 30°, (c) 45°,and (d) 60°.

Table 6
Simulation results with different angles of fiber inclination with the same microstructure under w/c ratio of 0.4. Average values are given with standard deviations in parentheses.

Angle of fiber inclination	τ_d (MPa)	τ_0 (MPa)	τ_f (MPa)	σ_f (MPa)	G_d (J/m^2)	β
0	3.00	1.57	9.92	495.88	1.07	2.00
	(0.59)	(0.36)	(1.18)	(59.04)	(0.43)	(0.47)
30	2.86	1.67	6.82	341.03	0.73	1.39
	(0.22)	(0.12)	(2.43)	(121.24)	(0.25)	(0.45)
45	1.60	0.88	7.32	365.92	0.27	3.46
	(0.40)	(0.25)	(2.15)	(107.46)	(0.11)	(1.99)
60	1.10	0.57	5.65	282.64	0.15	4.43
	(0.36)	(0.19)	(1.47)	(73.37)	(0.08)	(2.11)

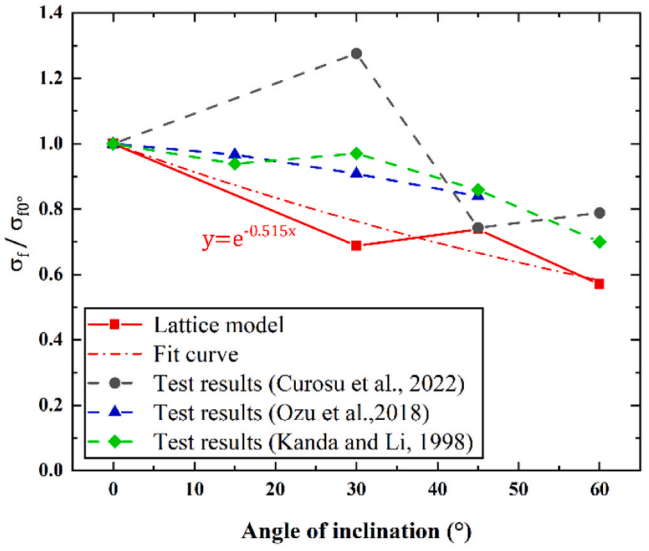

Fig. 13. Comparison with experiment results from literature on apparent pull-out strength ratio concerning fiber inclination angle at 0°. [3,19,50].

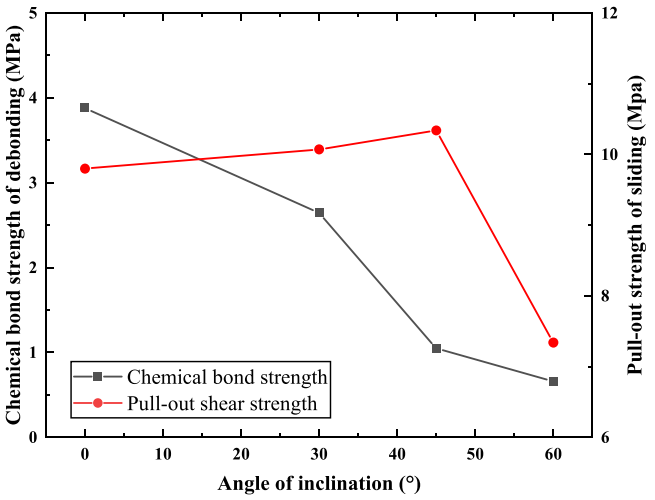

Fig. 14. The effect of inclination angle on chemical bond strength and frictional pull-out strength of FP1 with w/c ratio of 0.4.

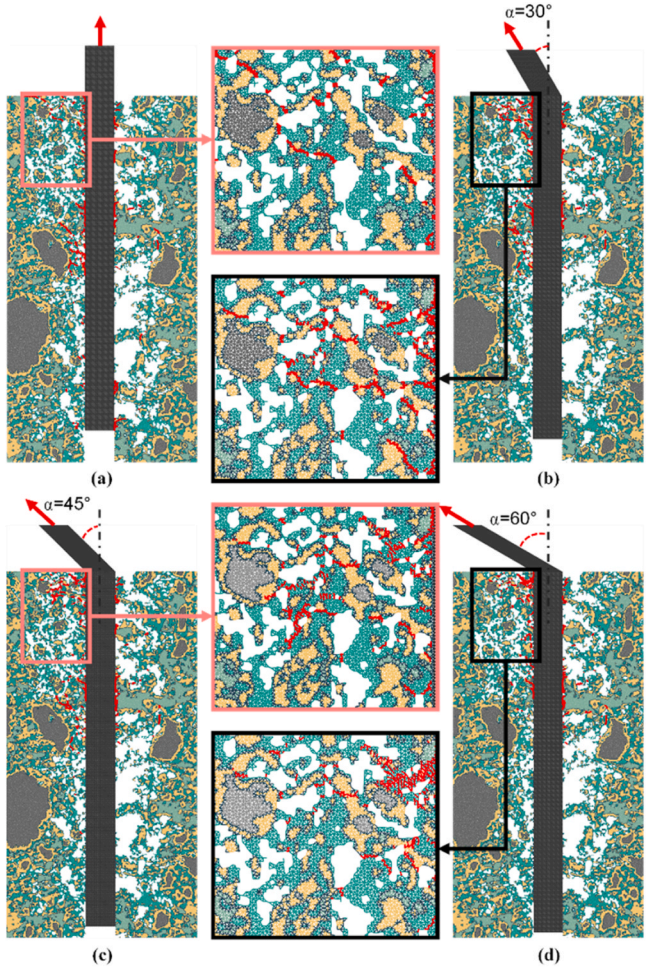

Fig. 15. Crack details in the ITZ of FP1 at slipping stage with w/c ratio of 0.4. Cracks are shown as red.

increasing inclination angle from 0° to 45° and then significantly decreases at the angle of 60°. Fig. 15 compares the crack patterns of model FP1 with different inclination angles at slipping stage. When the fiber is inclined, the pull-out load can be resolved into a horizontal force and a vertical force. Under the horizontal force, the matrix on one side of fiber

undergoes compression, and the other side experiences tension. When the porosity of microstructure at the compression zone is lower, with increasing angle of inclination, a higher pull-out strength is expected. As shown in Fig. 15(a), when the angle is 0°, the cracks in the matrix are mostly inclined. When the inclination angle is increased to 30° and 45°, the cracks become nearly parallel on the side subjected to compression, as shown in Fig. 15(b), (c). The cracks remain inclined in the area under vertical force. With the increasing load, the horizontal force is increased and resisted by matrix compression. Simultaneously, the vertical force is resisted by the matrix shear until shear fracture occurs. The combination of forces enhances the frictional pull-out strength. When the inclination angle increases to 60°, the horizontal force is also increased, causing the local region under compression to be crushed (see Fig. 15(d)). The pull-out load reaches its strength limit when the crushing occurs. Consequently, the fracture mode changes, with cracks mainly caused by the crushing of matrix. Additionally, few inclined cracks may from in other regions under vertical force generate due to the matrix crushing. The matrix spalling and fracture mode change were also observed in experiments as the angle of fiber inclination increased [51]. On the other side of fiber, the matrix under tension experiences the main fracture occurring at the surface of fiber.

Contrastingly, as depicted in Fig. 16, both the chemical bond strength and pull-out strength demonstrate a rapid decrease with increasing inclination angle. Noteworthy is the increased porosity observed in the ITZ near the load side, contributing to a microstructure susceptible to spalling, as illustrated in Fig. 17. The fracture patterns differ significantly from those observed in model FP1. As the load increases, the vertical force increases and is countered by matrix shear. At the same time, the horizontal force is resisted by matrix compression until a compression fracture occurs. With the increasing angle of inclination, the proportion of horizontal force also rises, resulting in a decrease in pull-out strength. In summary, the microstructure within the ITZ profoundly influences both the strength and fracture patterns observed with changes in fiber inclination.

4.4. Effect of bond strength

The chemical bond connecting the fiber and the matrix influences the debonding strength and frictional behaviors. Some researchers have modified the fiber surface to alter its hydrophilicity to achieve the enhancement and reduction of bond strength [20,23,52]. In the simulation, the strengthening or weakening of bond strength is accomplished by modifying the material properties of the interface elements. Herein,

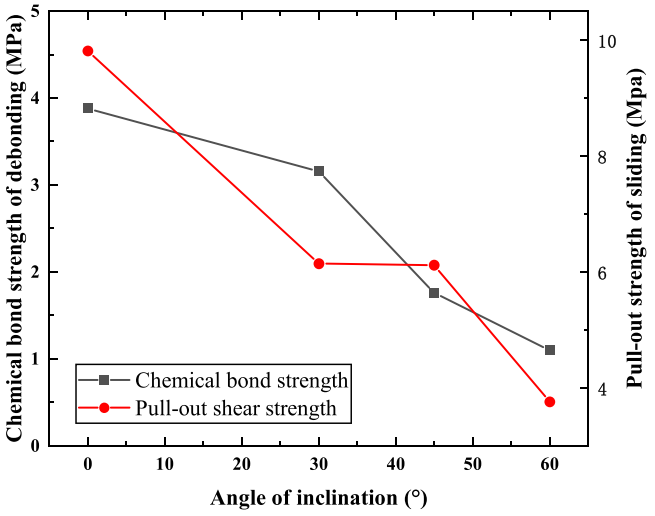

Fig. 16. The effect of inclination angle on chemical bond strength and frictional pull-out strength of FP5 with w/c ratio of 0.4.

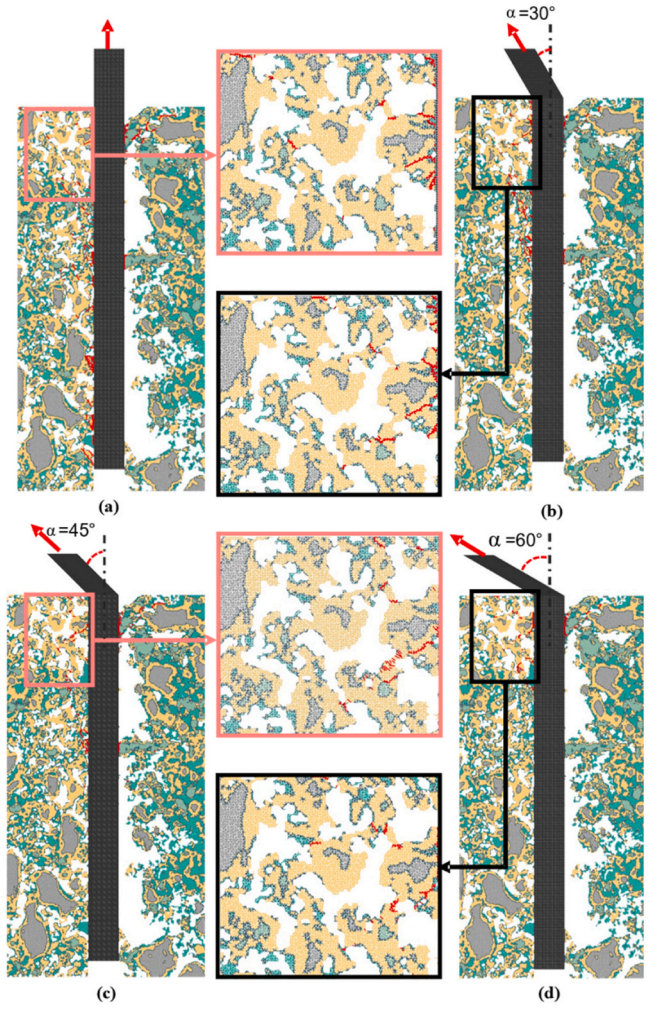

Fig. 17. Crack details in the ITZ of FP5 at slipping stage with w/c ratio of 0.4. Cracks are shown as red.

three types of bond strength were selected. The PVA fiber used in this paper features a 1.2 % oiling coating by weight, providing standard strength. A bond strength equivalent to 0.1 times the standard strength represents the bond strength provided by the PVA fiber with decreased bond strength due to excessively oiling coating or other methods. Similarly, a bond strength equivalent to 10 times the standard strength represents the bond strength provided by untreated PVA fiber or PVA fiber coated to increase bond strength. Models of specimen with those three bond strengths are established to analyze the influence of bond strength on fiber pull-out behaviors.

In Fig. 18, the chemical bond strength and fracture patterns for specimen FP2 with different bond strengths are presented. As expected, at debonding stage, the chemical bond strength increases with the increasing bond strength. For the fracture patterns, when the interface elements have the lowest strength, all the interface elements are ruptured. When the 1.2 % oiling coating PVA fiber is used, only a small number of fractures appear within the matrix. When the bond strength of the interface elements is set to 10 times of the standard strength, cracks extensively penetrate into the matrix, resulting in the spalling of the matrix. It should be noted that the specimen with the high bond strength might exhibit brittle behavior during slipping stage due to matrix spalling in ITZ. Conversely, with weak adhesion, the fiber might be smoothly pulled out, demonstrating strain-softening behavior. It is reported that untreated and excessively oiling coating PVA fibers may exhibit the low ductility in single fiber pull-out experiments, emphasizing the necessity of achieving a balance between debonding and pull-

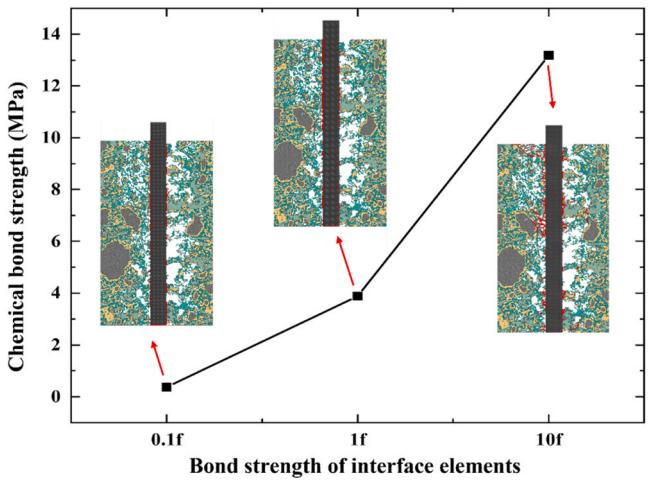

Fig. 18. The relationship of chemical bond strength and bond strength with w/c ratio of 0.4. Cracks are shown as red.

out to achieve better strain-hardening behavior [23,24,53].

5. Conclusions

An experimentally-informed lattice fracture model is established to simulate PVA fiber pull-out behaviors at the microscale. Single fiber pull-out testswere conducted to calibrate and validate the numerical model. Fracture patterns and the chemical bond strength, chemical bond energy during the debonding stage, as well as frictional pull-out strength and stress hardening during the slipping stage, were assessed.The influences of the w/c ratio, fiber inclination, and bond strength on the pull-out behavior were evaluated. Based on the obtained results, the following conclusion can be drawn:

1. Lattice model considers the real microstructure of ITZ and can accurately simulate the fiber pull-out behaviors with the 'birth-death' method. The simulated stress-strain curves agree well with the experimental results in terms of fracture properties, fracture pattern and stress-strain curves.
2. The ITZ microstructures affect the pull-out stress-strain response of fiber pull-out process by varying the fracture patterns at debonding and slipping stages.
3. There is a decreasing trend in the frictional pull-out strength with increasing angle of inclination. Also, it is found that the fracture modes of fiber pull-out transition from interface failure to matrix spalling with the increasing angle of fiber inclination. The change of fracture modes is associated with the matrix in the compression zone and the interface properties.
4. Enhanced bond strength allows the cracks extending into the matrix. The higher degree of damage in matrix might cause more brittle behavior of the fiber slipping stage.

Even though the microstructure-informed model can effectively predict the fiber pull-out behavior, the 2D model used in this paper cannot fully represent the actual microstructure and fracture patterns. Future studies should focus on 3D simulation of fiber pull-out behavior. Besides, the proposed model at microscale servers as the basis for further development in multiscale modeling of ECC. The behaviors of fiber pull-out can be utilized as constitutive law for mesoscopic model of ECC, and efforts could be directed towards upscaling the microscopic fiber pull-out behavior to interaction between fiber and matrix at the mesoscale.

CRediT authorship contribution statement

Branko Šavija: Writing – review & editing, Supervision, Methodology, Funding acquisition, Formal analysis, Conceptualization. **Shan He:** Writing – review & editing, Visualization, Resources, Methodology, Investigation, Data curation, Conceptualization. **Shen Yang:** Writing – review & editing, Writing – original draft, Validation, Software, Methodology, Investigation, Formal analysis, Data curation, Conceptualization. **Yidong Gan:** Writing – review & editing, Writing – original draft, Supervision, Software, Project administration, Methodology, Investigation, Formal analysis, Data curation.

Declaration of Competing Interest

The authors declare no conflict of interest.

Data availability

Data will be made available on request.

Acknowledgements

Yidong Gan would like to acknowledge the funding supported by Hubei Provincial Natural Science Foundation of China (Grant No.2024AFB562). Shan He acknowledges the financial supports from the MSCA-ITN Project SMARTINCS. This project has received funding from the European Union's Horizon 2020 Research and Innovation Programme under the Marie Skłodowska-Curie grant agreement No 860006. Also, Branko Šavija acknowledges the financial support of the European Research Council (ERC) within the framework of the ERC Starting Grant Project "Auxetic Cementitious Composites by 3D printing (ACC-3D)", Grant Agreement Number 101041342.

References

[1] K.Z. Farhan, M.A.M. Johari, R. Demirboğa, Impact of fiber reinforcements on properties of geopolymer composites: a review, J. Build. Eng. 44 (2021), https://doi.org/10.1016/j.jobe.2021.102628.
[2] M. Zhu, J. Zhang, B. Chen, M. Wu, J. Han, Numerical simulation of cost-effective green high-ductility engineered cementitious composites based on meso-scale particle flow model, Constr. Build. Mater. 356 (2022) 128973, https://doi.org/10.1016/j.conbuildmat.2022.128973.
[3] I. Curosu, E. Muja, M. Ismailov, A.H. Ahmed, M. Liebscher, V. Mechtcherine, An experimental-analytical scale-linking study on the crack-bridging mechanisms in different types of SHCC in dependence on fiber orientation, Cem. Concr. Res. 152 (2022) 106650, https://doi.org/10.1016/j.cemconres.2021.106650.
[4] M. Son, G. Kim, H. Kim, S. Lee, J. Nam, K. Kobayashi, Effects of the strain rate and fiber blending ratio on the tensile behavior of hooked steel fiber and polyvinyl alcohol fiber hybrid reinforced cementitious composites, Cem. Concr. Compos. 106 (2020) 103482, https://doi.org/10.1016/j.cemconcomp.2019.103482.
[5] D. Wang, C. Shi, Z. Wu, J. Xiao, Z. Huang, Z. Fang, A review on ultra high performance concrete: part II. Hydration, microstructure and properties, Constr. Build. Mater. 96 (2015) 368–377, https://doi.org/10.1016/j.conbuildmat.2015.08.095.
[6] V.M.C.F. Cunha, J.A.O. Barros, J.M. Sena-cruz, Pullout Behavior of Steel Fibers in Self-Compacting Concrete, 22 (2010) 1–9. https://doi.org/10.1061/(ASCE)MT.1943-5533.0000001.
[7] J. Gong, Y. Ma, J. Fu, J. Hu, X. Ouyang, Z. Zhang, H. Wang, Utilization of fibers in ultra-high performance concrete: a review, Compos. Part B Eng. 241 (2022) 109995, https://doi.org/10.1016/j.compositesb.2022.109995.
[8] J. Qi, Z. Wu, Z. John, J. Wang, Pullout behavior of straight and hooked-end steel fibers in UHPC matrix with various embedded angles, Constr. Build. Mater. 191 (2018) 764–774, https://doi.org/10.1016/j.conbuildmat.2018.10.067.
[9] K. Zhang, Q. Yuan, T. Huang, S. Zuo, H. Yao, Utilization of novel stranded steel fiber to enhance fiber – matrix interface of cementitious composites, Constr. Build. Mater. 369 (2023) 130525, https://doi.org/10.1016/j.conbuildmat.2023.130525.
[10] S. He, E.H. Yang, Strategic strengthening of the interfacial transition zone (ITZ) between microfiber and cement paste matrix with carbon nanofibers (CNFs), Cem. Concr. Compos. 119 (2021) 104019, https://doi.org/10.1016/j.cemconcomp.2021.104019.
[11] D.Y. Yoo, N. Banthia, S.T. Kang, Y.S. Yoon, Size effect in ultra-high-performance concrete beams, Eng. Fract. Mech. 157 (2016) 86–106, https://doi.org/10.1016/j.engfracmech.2016.02.009.
[12] K.L. Scrivener, A.K. Crumbie, P. Laugesen, The interfacial transition zone (ITZ) between cement paste and aggregate in concrete, Interface Sci. 12 (2004) 411–421, https://doi.org/10.1023/B:INTS.0000042339.92990.4c.
[13] Y. Lee, S.T. Kang, J.K. Kim, Pullout behavior of inclined steel fiber in an ultra-high strength cementitious matrix, Constr. Build. Mater. 24 (2010) 2030–2041, https://doi.org/10.1016/j.conbuildmat.2010.03.009.

[14] L. Huang, M. Yuan, B. Wei, D. Yan, Y. Liu, Experimental investigation on sing fiber pullout behaviour on steel fiber-matrix of reactive powder concrete (RPC), Constr. Build. Mater. 318 (2022) 125899, https://doi.org/10.1016/j.conbuildmat.2021.125899.
[15] K. Wille, A.E. Naaman, Pullout behavior of high-strength steel fibers embedded in ultra-high-performance concrete, Acids Mater. J. 109 (2012) 479–488, https://doi.org/10.14359/51683923.
[16] Z. Pi, H. Xiao, J. Du, C. Li, W. Cai, M. Liu, Effect of the water/cement ratio on the improvement of pullout behaviors using nano-SiO2 modified steel fiber and the micro mechanism, Constr. Build. Mater. 338 (2022) 127632, https://doi.org/10.1016/j.conbuildmat.2022.127632.
[17] J. Zhang, V.C. Li, Effect of inclination angle on fiber rupture load in fiber reinforced cementitious composites, Compos. Sci. Technol. 62 (2002) 775–781, https://doi.org/10.1016/S0266-3538(02)00045-3.
[18] R.B. Jewell, K.C. Mahboub, T.L. Robl, A.C. Bathke, Interfacial bond between reinforcing fibers and calcium sulfoaluminate cements: fiber pullout characteristics, Acids Mater. J. 112 (2015) 39–48, https://doi.org/10.14359/51687234.
[19] T. Kanda, V.C. Li, Interface property and apparent strength of high-strength hydrophilic fiber in cement matrix, J. Mater. Civ. Eng. 10 (1998) 5–13, https://doi.org/10.1061/(asce)0899-1561(1998)10:1(5).
[20] C. Redon, V.C. Li, Measuring and modifying interface properties of pva fibers in eCC Matrix, Manager (2001) 399–406.
[21] F. Isla, G. Ruano, B. Luccioni, Analysis of steel fibers pull-out. Experimental study, Constr. Build. Mater. 100 (2015) 183–193, https://doi.org/10.1016/j.conbuildmat.2015.09.034.
[22] V.C. Li, C. Wu, S. Wang, A. Ogawa, T. Saito, Interface tailoring for strain-hardening polyvinyl alcohol-engineered cementitious composite (PVA-ECC), Acids Mater. J. 99 (2002) 463–472, https://doi.org/10.14359/12325.
[23] M.F. Arain, M. Wang, J. Chen, H. Zhang, Study on PVA fiber surface modification for strain-hardening cementitious composites (PVA-SHCC), Constr. Build. Mater. 197 (2019) 107–116, https://doi.org/10.1016/j.conbuildmat.2018.11.072.
[24] I. Curosu, M. Liebscher, G. Alsous, E. Muja, H. Li, A. Drechsler, R. Frenzel, A. Synytska, V. Mechtcherine, Tailoring the crack-bridging behavior of strain-hardening cement-based composites (SHCC) by chemical surface modification of poly(vinyl alcohol) (PVA) fibers, Cem. Concr. Compos. 114 (2020) 103722, https://doi.org/10.1016/j.cemconcomp.2020.103722.
[25] H. Li, D. Zhao, M. Liebscher, B. Yin, J. Yang, M. Kaliske, V. Mechtcherine, An experimental and numerical study on the age depended bond-slip behavior between nano-silica modified carbon fibers and cementitious matrices, Cem. Concr. Compos. 128 (2022) 104416, https://doi.org/10.1016/j.cemconcomp.2022.104416.
[26] F. Isla, P. Argañaraz, B. Luccioni, Numerical modelling of steel fibers pull-out from cementitious matrixes, Constr. Build. Mater. 332 (2022), https://doi.org/10.1016/j.conbuildmat.2022.127373.
[27] G. Lin, P.H. Geubelle, N.R. Sottos, Simulation of fiber debonding with friction in a model composite pushout test, Int. J. Solids Struct. 38 (2001) 8547–8562, https://doi.org/10.1016/S0020-7683(01)00085-3.
[28] J.H. Tsai, A. Patra, R. Wetherhold, Finite element simulation of shaped ductile fiber pullout using a mixed cohesive zone/friction interface model, Compos. Part A Appl. Sci. Manuf. 36 (2005) 827–838, https://doi.org/10.1016/j.compositesa.2004.10.025.
[29] C.Y. Li, B. Mobasher, Finite element simulations of fiber pullout toughening in fiber reinforced cement based composites, Adv. Cem. Based Mater. 7 (1998) 123–132, https://doi.org/10.1016/S1065-7355(97)00087-4.
[30] B.D. Ellis, D.L. McDowell, M. Zhou, Simulation of single fiber pullout response with account of fiber morphology, Cem. Concr. Compos. 48 (2014) 42–52, https://doi.org/10.1016/j.cemconcomp.2014.01.003.
[31] S.S. Mukrimaa, Nurdyansyah, E.F. Fahyuni, A. Yulia Citra, N.D. Schulz, د. غسان, T. Taniredja, E.M. Faridli, S. Harmianto, Microstructural characteristics and their impact on mechanical properties of steel-PVA fiber reinforced concrete, J. Penelit. Pendidik. Guru Sekol. Dasar 6 (2016) 128.
[32] S.F. Lee, S. Jacobsen, Study of interfacial microstructure, fracture energy, compressive energy and debonding load of steel fiber-reinforced mortar, Mater. Struct. Constr. 44 (2011) 1451–1465, https://doi.org/10.1617/s11527-011-9710-4.
[33] Y. Gan, M. Vandamme, Y. Chen, E. Schlangen, K. van Breugel, B. Šavija, Experimental investigation of the short-term creep recovery of hardened cement paste at micrometre length scale, Cem. Concr. Res. 149 (2021) 106562, https://doi.org/10.1016/j.cemconres.2021.106562.
[34] Y. Gan, H. Zhang, Y. Zhang, Y. Xu, E. Schlangen, K. van Breugel, B. Šavija, Experimental study of flexural fatigue behaviour of cement paste at the microscale, Int. J. Fatigue 151 (2021) 106378, https://doi.org/10.1016/j.ijfatigue.2021.106378.
[35] Y. Gan, C.R. Rodriguez, E. Schlangen, K. van Breugel, B. Šavija, Assessing strain rate sensitivity of cement paste at the micro-scale through micro-cantilever testing, Cem. Concr. Compos. 121 (2021) 104084, https://doi.org/10.1016/j.cemconcomp.2021.104084.
[36] M. Luković, E. Schlangen, G. Ye, Combined experimental and numerical study of fracture behaviour of cement paste at the microlevel, Cem. Concr. Res. 73 (2015) 123–135, https://doi.org/10.1016/j.cemconres.2015.03.008.
[37] H. Zhang, B. Šavija, S.C. Figueiredo, M. Lukovic, E. Schlangen, Microscale testing and modelling of cement paste as basis for multi-scale modelling, Materials 9 (2016), https://doi.org/10.3390/ma9110907.
[38] Y. Gan, C. Romero Rodriguez, H. Zhang, E. Schlangen, K. van Breugel, B. Šavija, Modeling of microstructural effects on the creep of hardened cement paste using an experimentally informed lattice model, Comput. Civ. Infrastruct. Eng. 36 (2021) 560–576, https://doi.org/10.1111/mice.12659.
[39] S. He, S. Zhang, M. Luković, E. Schlangen, Effects of bacteria-embedded polylactic acid (PLA) capsules on fracture properties of strain hardening cementitious composite (SHCC), Eng. Fract. Mech. 268 (2022), https://doi.org/10.1016/j.engfracmech.2022.108480.
[40] S. He, Y. Chen, M. Liang, E.H. Yang, E. Schlangen, Distribution of porosity surrounding a microfiber in cement paste, Cem. Concr. Compos. 142 (2023) 105188, https://doi.org/10.1016/j.cemconcomp.2023.105188.
[41] T.K.Z.Lin, On interface property characterization and performance of fiber reinforced cementitious composites, (n.d.).
[42] M. Liang, S. He, Y. Gan, H. Zhang, Z. Chang, E. Schlangen, B. Šavija, Predicting micromechanical properties of cement paste from backscattered electron (BSE) images by computer vision, Mater. Des. 229 (2023) 111905, https://doi.org/10.1016/j.matdes.2023.111905.
[43] Y. Li, W. Guo, H. Li, Quantitative analysis on ground blast furnace slag behavior in hardened cement pastes based on backscattered electron imaging and image analysis technology, Constr. Build. Mater. 110 (2016) 48–53, https://doi.org/10.1016/j.conbuildmat.2016.02.015.
[44] H.S. Wong, M.K. Head, N.R. Buenfeld, Pore segmentation of cement-based materials from backscattered electron images, Cem. Concr. Res. 36 (2006) 1083–1090, https://doi.org/10.1016/j.cemconres.2005.10.006.
[45] H.S. Wong, N.R. Buenfeld, Determining the water-cement ratio, cement content, water content and degree of hydration of hardened cement paste: Method development and validation on paste samples, Cem. Concr. Res. 39 (2009) 957–965, https://doi.org/10.1016/j.cemconres.2009.06.013.
[46] Y. Liu, Y. Wang, J. Zhang, in: B. Liu, M. Ma, J. Chang (Eds.), New Machine Learning Algorithm: Random Forest BT - Information Computing and Applications, Springer Berlin Heidelberg, Berlin, Heidelberg, 2012, pp. 246–252.
[47] M.H. Zhang, O.E. Gjørv, Effect of silica fume on cement hydration in low porosity cement pastes, Cem. Concr. Res. 21 (1991) 800–808, https://doi.org/10.1016/0008-8846(91)90175-H.
[48] N.X. Randall, M. Vandamme, F.J. Ulm, Nanoindentation analysis as a two-dimensional tool for mapping the mechanical properties of complex surfaces, J. Mater. Res. 24 (2009) 679–690, https://doi.org/10.1557/jmr.2009.0149.
[49] E. Giordano, M.G. Masciotta, F. Clementi, B. Ghiassi, Numerical prediction of the mechanical behavior of TRM composites and TRM-strengthened masonry panels, Constr. Build. Mater. 397 (2023) 132376, https://doi.org/10.1016/j.conbuildmat.2023.132376.
[50] Y. Ozu, H. Yamada, A. Yasojima, T. Kanakubo, in: V. Mechtcherine, V. Slowik, P. Kabele (Eds.), Evaluation of Shear and Tensile Bridging Characteristics of PVA Fibers Based on Bridging Law, Springer Netherlands, Dordrecht, 2018, pp. 88–96, https://doi.org/10.1007/978-94-024-1194-2_10.
[51] D.Y. Yoo, S. Kim, Comparative pullout behavior of half-hooked and commercial steel fibers embedded in UHPC under static and impact loads, Cem. Concr. Compos. 97 (2019) 89–106, https://doi.org/10.1016/j.cemconcomp.2018.12.023.
[52] Y. Zhou, J. Huang, X. Yang, Y. Dong, T. Feng, J. Liu, Enhancing the PVA fiber-matrix interface properties in ultra high performance concrete: an experimental and molecular dynamics study, Constr. Build. Mater. 285 (2021) 122862, https://doi.org/10.1016/j.conbuildmat.2021.122862.
[53] Z. Pan, Z. Qiao, D. Si, J. Shang, Experimental investigation and numerical simulation on uniaxial tensile behavior of hybrid PVA-ECC, Constr. Build. Mater. 398 (2023) 132517, https://doi.org/10.1016/j.conbuildmat.2023.132517.